Official URL: https://doi.org/10.2514/1.J060792

To cite this version :

Rolandi, Laura Victoria and Jardin, Thierry and Fontane, Jérôme and Gressier, Jérémie and Joly, Laurent Stability of the Low Reynolds Number Compressible Flow Past a NACA0012 Airfoil. (2021) AIAA Journal. ISSN 0001-1452

Stability of the Low Reynolds Number Compressible Flow Past a NACA0012 Airfoil

Laura Victoria Rolandi,[*] Thierry Jardin,[†] Jérôme Fontane,[‡] Jérémie Gressier,[§]
and Laurent Joly[¶]
ISAE-SUPAERO, University of Toulouse, 31055 France

https://doi.org/10.2514/1.J060792

With stratospheric flight or martian exploration in perspective, the compressibility influence on the wake dynamics of a NACA0012 profile is investigated. The unsteady flow past the airfoil at $Re = 1000$ is characterized using direct numerical simulations for various angles of attack $\alpha \in [0°; 20°]$ and Mach numbers up to $M_\infty = 0.5$. Steady flows obtained using the selective frequency damping (SFD) technique are used as base states for a global linear stability analysis. The influence of both the angle of attack and the Reynolds number on the most amplified mode characteristics is first investigated in the incompressible regime. Then, the compressibility effects in the subcritical regime are considered. A stabilizing or a destabilizing effect of compressibility is observed depending on the angle of attack and the Reynolds number. For $\alpha < 20°$, compressibility has a destabilizing effect close to the critical threshold, which results in an earlier Hopf bifurcation, whereas increasing the Mach number always results in a decrease of the growth rate of the mode well above the critical threshold. Finally, the mode frequency decreases with the Mach number.

Nomenclature

$\mathcal{K}_m$ = Krylov subspace of dimension m
$\mathcal{L}$ = Jacobian matrix of the Navier–Stokes operator
$\mathcal{M}$ = propagator, $\exp(\mathcal{L}t)$
M_∞ = Mach number
$\boldsymbol{q}$ = state vector, $(\rho, \rho\boldsymbol{u}, \rho E)$
$\boldsymbol{q}_b$ = base state
$\boldsymbol{q}'$ = disturbance of the state vector, $\tilde{\boldsymbol{q}}\exp(\omega t)$
$\tilde{\boldsymbol{q}}$ = eigenvector, $(\tilde{\rho}, \widetilde{\rho\boldsymbol{u}}, \widetilde{\rho E})$
$\boldsymbol{q}_+^\tau$ = direct numerical simulation solution at t is equal to τ starting from initial condition $(\boldsymbol{q}_b + \epsilon\boldsymbol{q}')$
$\boldsymbol{q}_-^\tau$ = direct numerical simulation solution at t is equal to τ starting from initial condition $(\boldsymbol{q}_b - \epsilon\boldsymbol{q}')$
Re = Reynolds number
St = Strouhal number
α = angle of attack
Δ = temporal filter width
χ = gain coefficient
ω = eigenvalue, $\omega_r + i\omega_i$
ω_i = mode frequency
ω_r = growth rate

I. Introduction

COMPRESSIBLE flows at low Reynolds numbers have recently gained significant interest in many prospective applications, such as vactrains (e.g., hyperloop concept), stratospheric flight, martian exploration, and optimization of liquid atomization. These flows are generally typical of low-density/pressure environments or high-speed micro-objects. Despite its importance in a growing number of engineering applications, fundamental knowledge on the physics underlying low-Reynolds-number compressible flows is lacking. In addition to those practical perspectives, the analysis of compressibility effects under low-Reynolds-number condition could help understand more complex mechanisms at higher Reynolds numbers. For example, as suggested by Meliga et al. [1], the analysis of vortex shedding phenomenon at low Reynolds numbers could be a key point for understanding transition to turbulence, because the von Kármán vortex street persists at higher Reynolds numbers in the fully developed turbulent regime [2].

Recently, some studies have been conducted on the effect of compressibility on the stability of low-Reynolds-number flows [1,3,4]. In their global stability analysis of axisymmetric two-dimensional (2D) wake flows, Meliga et al. [1] reported contrasted effects of compressibility in the subsonic regime (up to $M_\infty = 0.7$), depending on the base flow configuration. Focusing on the secondary Hopf bifurcation, they observed an increase of the critical Reynolds number at which the secondary oscillating helical mode becomes unstable with respect to the Mach number in the case of an axisymmetric afterbody flow at zero angle of attack, hence a stabilizing effect of compressibility. Conversely, they observed a decrease of the same critical Reynolds number with respect to the Mach number, up to $M_\infty \approx 0.63$, for the flow around a sphere. Through an adjoint-based sensitivity analysis, they related this stabilizing/destabilizing behavior to a change in the longitudinal advection of the perturbation by the base flow within the recirculation zone in the lee of the body. Their analysis questions the previous hypothesis of Bouhadji and Braza [5], who attributed the destabilizing effect of compressibility to an increase of the length of the recirculation bubble, whereas this lengthening is observed for both the afterbody and the sphere in [1].

The increase of the recirculation length with growing Mach number has also been documented by Canuto and Taira [3] for the flow around a circular cylinder and by Sansica et al. [4] for the sphere, with a stronger elongation as the critical Reynolds number is approached. In the latter case, the recirculation length is significantly reduced as M_∞ increases above unity (see also [6,7]). The size variation of the separation regions behind bodies influences the natural frequency of the flow [6–9], as well as the frequency of the most unstable mode [4]. In both [3,4], the frequency of the most amplified eigenmode is found to decrease as the recirculation length increases.

Sansica et al. also extended the stability analysis of Meliga for the sphere up to low supersonic regime at $M_\infty = 1.2$, for Reynolds numbers between $Re = 200$ and $Re = 370$. Considering a three-dimensional (3D) base flow, they confirmed the non-monotonic effect of compressibility but observed a destabilization only in the low subsonic regime up to $M_\infty \approx 0.3$. For higher Mach numbers, the

---

[*] Ph.D. Student; currently Department of Aerodynamics, Energetics and Propulsion; laura-victoria.rolandi@isae-supaero.fr.

[†] Research Engineer, Department of Aerodynamics, Energetics and Propulsion; thierry.jardin@isae-supaero.fr.

[‡] Associate Professor, Department of Aerodynamics, Energetics and Propulsion; jerome.fontane@isae-supaero.fr.

[§] Associate Professor, Department of Aerodynamics, Energetics and Propulsion; jeremie.gressier@isae-supaero.fr.

[¶] Professor, Department of Aerodynamics, Energetics and Propulsion; laurent.joly@isae-supaero.fr.

helical oscillating mode is progressively damped until its complete stabilization in the high subsonic regime ($M_\infty \approx 0.7$ for $Re = 280$). They attributed this difference to the base flow axisymmetry assumption used by Meliga et al.

This specific regime of compressible low-Reynolds-number flows has also been investigated experimentally in the Mars Wind Tunnel at Tohoku University. Anyoji et al. [10] compared the aerodynamic characteristics of a flat plate and a NACA0012-34 airfoil at Reynolds numbers $Re \in [4300; 41{,}000]$ in the low subsonic regime, up to $M_\infty = 0.6$. Effects of compressibility on the aerodynamic coefficients at Reynolds numbers in the range $Re \in [100; 10{,}000]$ have been also studied in [11–14] for flat plates, cambered and triangular airfoils. From these studies, it can be concluded that for Reynolds numbers up to $Re \approx 10{,}000$, the influence of compressibility on the drag and lift coefficients is not the same for the different angles of attack tested. In particular, the dynamics of the separated leading-edge shear layer at high angles of attack is highly dependent on the Mach number, which affects leading-edge vortex formation and the resulting aerodynamic force. Unique features related to the displacement of the shock foot away from the airfoil surface were also put into evidence in the transonic regime [13]. Yet, despite these few studies, fundamental knowledge on the occurrence of instabilities in the compressible flow past airfoils at low Reynolds numbers is still lacking. In this regard, the objective of this work is to investigate compressibility effects on the wake dynamics of a 2D NACA0012 profile through a global linear modal stability analysis [15,16] combined with direct numerical simulations (DNS). In particular, our study is focused on the first bifurcation in order to detail how the characteristics of the most unstable mode and the associated critical Reynolds number are affected by compressibility effects.

The choice of the base flow on which the global stability analysis is performed is of crucial importance. Indeed, in their work, Sansica et al. showed the different stability responses to the base flow choice: mean flow versus fixed point solution. As originally found by Barkley [17] in the case of the circular cylinder, before being theoretically proven by Sipp and Lebedev [18] and generalized by Turton et al. [19], temporal averages of quasi-monochromatic frequency oscillating flows are marginally stable close to critical parameters, rendering the identification of bifurcation threshold impossible, while the mode frequency matches the natural one. On the other hand, stability analysis performed on actual base flows (obtained with fixed point, filtered, or enforced symmetric solutions) enables a clear identification of the critical threshold, but the mode frequency diverges from the observed one when moving above the bifurcation threshold. Because the present work focuses on the influence of the Mach number on the first bifurcation, we opt for a base flow defined as a fixed point solution of Navier–Stokes equations.

The paper is structured as follows. The numerical approaches used for the base flow computation and for the global stability analysis are presented in Sec. II. In Sec. III results from stability analysis and DNS on the NACA0012 airfoil are discussed for both the incompressible and compressible flow regimes, with angles of attack ranging from $\alpha = 8°$ to $\alpha = 20°$ and Reynolds numbers up to $Re = 1000$. Conclusions and perspectives are reported in Sec. IV.

II. Numerical Methods

A. Governing Equations

We consider the 3D compressible Navier–Stokes (NS) equations in conservative form for an ideal gas:

$$
\begin{aligned}
&\frac{\partial \rho}{\partial t} + \nabla \cdot (\rho \boldsymbol{u}) = 0 \\
&\frac{\partial \rho \boldsymbol{u}}{\partial t} + \nabla \cdot (\rho \boldsymbol{u} \otimes \boldsymbol{u}) = -\nabla p + \nabla \cdot \left[\mu (\nabla \boldsymbol{u} + \nabla \boldsymbol{u}^T) - \frac{2}{3} \mu \nabla \cdot \boldsymbol{u} \delta_{ij} \right] \\
&\frac{\partial \rho E}{\partial t} + \nabla \cdot (\rho \boldsymbol{u} E + p \boldsymbol{u}) = \nabla \cdot (K \nabla T) + \nabla \cdot \left(\boldsymbol{u} \left[\mu (\nabla \boldsymbol{u} + \nabla \boldsymbol{u}^T) \right.\right. \\
&\qquad \left.\left. - \frac{2}{3} \mu \nabla \cdot \boldsymbol{u} \delta_{ij} \right] \right)
\end{aligned}
\tag{1}
$$

where ρ is the fluid density, $\boldsymbol{u}$ the velocity vector, p the pressure, T the temperature, and E the total energy. The viscosity μ and the thermal conductivity K are constant. The system can be written in the following compact form:

$$
\frac{\partial \boldsymbol{q}}{\partial t} = \mathcal{N}(\boldsymbol{q}) \tag{2}
$$

with $\boldsymbol{q} = (\rho, \rho \boldsymbol{u}, \rho E)^{\mathrm{T}}$ representing the state vector and $\mathcal{N}$ the nonlinear Navier–Stokes dynamic operator. We introduce the four nondimensional numbers:

$$
Re = \frac{\rho_\infty U_\infty L}{\mu}, \quad M_\infty = \frac{U_\infty}{\sqrt{\gamma \frac{p_\infty}{\rho_\infty}}}, \quad St = \frac{fL}{U_\infty}, \quad Pr = \frac{\mu c_p}{K} \tag{3}
$$

the Reynolds number, Mach number, Strouhal number, and Prandtl number, respectively. Here, the Prandtl number is taken constant ($Pr = 0.7$). Quantities with subscript$_\infty$ indicate upstream quantities, L is a characteristic length scale, c_p is the specific heat at constant pressure, γ is the ratio of specific heats, and f is the frequency. The corresponding characteristic time scale is $T = L/U_\infty$.

B. Base State Computation

The steady base flow is obtained with the numerical solver IC3, a high-order compact compressible code developed at ISAE-SUPAERO [20,21]. IC3 is a parallel finite-volume-based code with explicit Runge–Kutta (RK) scheme for time integration. In this work, the third-order RK and the fourth-order centered schemes have been used, respectively, for temporal and spatial discretization.

Below the critical threshold of the first bifurcation, the base flow corresponds to a steady solution of NS equations that is directly obtained from DNS. Above the critical threshold, the numerically simulated flow is naturally unsteady, and there are two options to force a steady base flow required for the stability analysis. Either it can be chosen as the time average of the unsteady solution, or the steadiness of the numerical solution can be enforced. As discussed in the Introduction, the former is better suited for the prediction of the natural frequency, whereas the latter gives the correct critical threshold and the growth rate of the unstable mode. As we are interested in the influence of compressibility on the first bifurcation, we opt for the second option and resort to a filtering technique.

We use the selective frequency damping (SFD) method, first introduced by Åkervik et al. [22], which damps the highest temporal frequency modifying the Navier–Stokes equations (2) in the following way:

$$
\begin{aligned}
\frac{\partial \boldsymbol{q}}{\partial t} &= \mathcal{N}(\boldsymbol{q}) - \chi (\boldsymbol{q} - \bar{\boldsymbol{q}}) \\
\frac{\partial \bar{\boldsymbol{q}}}{\partial t} &= \frac{\boldsymbol{q} - \bar{\boldsymbol{q}}}{\Delta}
\end{aligned}
\tag{4}
$$

where χ is a control coefficient and $\bar{\boldsymbol{q}}$ an approximation of the unknown steady solution computed at each iteration by applying a low pass filter of width Δ to the solution $\boldsymbol{q}$. Both $\boldsymbol{q}$ and $\bar{\boldsymbol{q}}$ converge toward the targeted steady solution $\bar{\boldsymbol{q}}_0$, i.e., $\mathcal{N}(\bar{\boldsymbol{q}}_0) = 0$.

The filter cutoff frequency $f_c = (1/\Delta)$ must be chosen below the frequency of the unstable disturbance of the flow. Considering ω as the most unstable eigenvalue of the unfiltered dynamic system, the control coefficient has to satisfy $\omega_r < \chi < \omega_r + f_c$, where ω_r represents the growth rate [22]. Besides, χ must be large enough to force the relaxation of the system toward $\bar{q}$, but not that large to impact the convergence. Close to the bifurcation threshold, one can consider that $\omega_r \ll f_c$; therefore $\chi = f_c$ stands as a good compromise. Despite its ease of implementation, this method presents some limitations: it does not converge for any arbitrary (Δ, χ) pairs and the convergence toward the steady-state solution can be very long; see also [23]. In this work, the filter parameters (Δ, χ) are deduced from unfiltered DNS solutions: $\Delta = (1/f_n)$ and $\chi = (1/\Delta)$, where f_n is the natural frequency of the oscillating wake. The simulation is considered converged to the equilibrium state at some time t_f when the relative variation of the momentum L2-norm stays below 0.2% during five characteristic times, namely:

$$\frac{\|\rho\boldsymbol{u}(t) - \rho\boldsymbol{u}(t_f - 5T)\|_2}{\|\rho\boldsymbol{u}(t_f - 5T)\|_2} \leq 0.002 \qquad \text{for } t \in [t_f - 5T; t_f]$$

C. Stability Analysis

Linear dynamics is based on the assumption that in a small neighborhood of a state $\boldsymbol{q}$, the dynamics of the nonlinear system $\dot{\boldsymbol{q}} = \mathcal{N}(\boldsymbol{q})$ is characterized by the dynamics of the linearized system:

$$\begin{aligned}\frac{\partial(\boldsymbol{q} + \epsilon\boldsymbol{q}')}{\partial t} &= \mathcal{N}(\boldsymbol{q} + \epsilon\boldsymbol{q}') \\ &= \mathcal{N}(\boldsymbol{q}) + \epsilon\left.\frac{\partial\mathcal{N}(\boldsymbol{q})}{\partial\boldsymbol{q}}\right|_{\boldsymbol{q}}\boldsymbol{q}' + O(\epsilon^2)\end{aligned} \tag{5}$$

where $\epsilon \ll 1$. Therefore, the dynamics of a perturbation $\boldsymbol{q}' = \tilde{\boldsymbol{q}}e^{\omega t}$, with $\tilde{\boldsymbol{q}} = [\tilde{\rho}, \tilde{\rho\boldsymbol{u}}, \tilde{\rho E}]^T$, in the neighborhood of the base state $\boldsymbol{q}_b$ reads

$$\frac{\partial\boldsymbol{q}'}{\partial t} = \mathcal{L}\boldsymbol{q}' \tag{6}$$

where $\mathcal{L} = \frac{\partial\mathcal{N}(\boldsymbol{q})}{\partial\boldsymbol{q}}\big|_{\boldsymbol{q}_b}$ is the Jacobian matrix of the Navier–Stokes operator computed at the base state $\boldsymbol{q}_b$. To find the dominant modes that govern the asymptotic behavior of the perturbation, we have to compute the spectrum of $\mathcal{L}$. Explicitly assembling the Jacobian matrix of very-large-scale dynamic systems can be very expensive and time-consuming. For this reason, the so-called matrix-free approaches are becoming very popular nowadays: the coefficients of the Jacobian matrix are not computed explicitly, but rather accessed by evaluating matrix–vector products. Many iterative methods for solving eigenvalue problems allow a matrix-free implementation, including the Krylov–Schur method [24] that has been chosen here. This method belongs to the class of Krylov projection methods whose aim is to find an approximation of the most relevant Ritz pairs of a matrix, projecting the original problem onto an orthonormal basis of the Krylov subspace.

Given the eigenproblem

$$A\boldsymbol{x} = \lambda\boldsymbol{x} \tag{7}$$

the Krylov subspace of m-dimension $\mathcal{K}_m$ is generated by the $n \times n$ matrix A and an n-vector $\boldsymbol{b}$ as follows:

$$\mathcal{K}_m = \mathrm{span}\{\boldsymbol{b}, A\boldsymbol{b}, A^2\boldsymbol{b}, \ldots, A^{m-1}\boldsymbol{b}\} \tag{8}$$

where $\{\boldsymbol{b}, A\boldsymbol{b}, A^2\boldsymbol{b}, \ldots, A^{m-1}\boldsymbol{b}\}$ is called the Krylov sequence. This sequence, under certain assumptions, converges toward the eigenvector associated with the largest modulus eigenvalue as $m \to \infty$ (power iteration method).

The Krylov–Schur method is an improvement of the Arnoldi algorithm, whose main steps can be found in [25,26]. Considering the problem (7) and the Krylov sequence, we can write

$$A\mathcal{K}_m \simeq \mathcal{K}_m\underbrace{[\boldsymbol{e}_2, \boldsymbol{e}_3, \ldots, \boldsymbol{e}_m, -\boldsymbol{c}]}_{\text{Companion matrix}} \tag{9}$$

The computation of the companion matrix spectrum is cheaper than that of A and, since the companion matrix represents the projection of A into $\mathcal{K}_m$, its eigenpairs approximate those of A. Approximation (9) can be reformulated as follows:

$$A\mathcal{V}_m = \mathcal{V}_m\mathcal{H} + \underbrace{\boldsymbol{r}\boldsymbol{e}_m^T}_{\text{residual}} \tag{10}$$

where $\mathcal{V}_m$ is an orthonormal basis of the Krylov subspace, normalized with the Euclidean norm. $\mathcal{H}$ is an upper Hessenberg matrix whose spectrum approximates that of A and the residual indicates how far the orthonormal basis is from an invariant subspace of A [26]. Once the eigenpairs of $\mathcal{H}$ have been computed, those of A are given by $(\lambda_A, \boldsymbol{x}_A) \simeq (\lambda_{\mathcal{H}}, \mathcal{V}_m\boldsymbol{x}_{\mathcal{H}})$. The main difference between Arnoldi and Krylov–Schur methods lies in the number of iterations m required to ensure the convergence of a given number of eigenvalues : m may be too large when using the Arnoldi method. This can yield very large matrices that exceed the available memory and considerably increase the cost of computing $\mathcal{H}_m$-eigenpairs (the cost grows cubically with m). The Krylov–Schur method, instead, incorporates an effective restarting scheme, which fixes the dimension of the Krylov subspace and iteratively applies the Arnoldi factorization. More precisely, if k eigenpairs are needed, the Krylov subspace dimension is fixed so that $m > k$, the m-Arnoldi factorization is called, and if k eigenpairs have not converged yet, the unwanted part of the factorization is discarded in order to restart the process with the remaining eigenvectors as the new initial Krylov subspace [26]. The matrix-free formulation can be used in Arnoldi-based algorithms because an explicit representation of the Jacobian matrix is not necessary. Only matrix–vector products are needed for the construction of the Krylov subspace.

This method is implemented by coupling the software library SLEPc for the solution of large-scale sparse eigenvalue problems, which has proven to perform better than ARPACK [26], with our computational fluid dynamics (CFD) solver IC3 for a time-stepping matrix-free exponential transformation using full DNS, as first introduced by Chiba [27], Tezuka and Suzuki [28], and Tezuka [29]. Considering the dynamics of the perturbation given by Eq. (6) and an initial condition $\boldsymbol{q}'(0)$, the analytic solution at time t is

$$\boldsymbol{q}'(t) = \mathcal{M}\boldsymbol{q}'(0)$$

where $\mathcal{M} = e^{\mathcal{L}t}$ is the exponential propagator. Applying Arnoldi-based algorithms on $\mathcal{M}$ instead of $\mathcal{L}$ is usually preferable, because Arnoldi-based algorithms converge toward the eigenvectors associated with the eigenvalues of largest modulus that may not correspond to the most amplified modes, i.e., the eigenvalues with the largest real part.

In Chiba's algorithm, $\mathcal{M}\boldsymbol{q}'$ is approximated as follows:

$$\mathcal{M}\boldsymbol{q}' = \frac{\boldsymbol{q}_+^\tau - \boldsymbol{q}_-^\tau}{2\epsilon} \tag{11}$$

where $\boldsymbol{q}_+^\tau$ and $\boldsymbol{q}_-^\tau$ are the DNS solutions corresponding to the initial conditions $(\boldsymbol{q}_b + \epsilon\boldsymbol{q}')$ and $(\boldsymbol{q}_b - \epsilon\boldsymbol{q}')$ integrated until τ. The same numerical parameters used for the base state computation have been used for the computation of $\boldsymbol{q}_+^\tau$ and $\boldsymbol{q}_-^\tau$.

Once the eigenpairs $(\lambda_{\mathcal{M}}, \boldsymbol{x}_{\mathcal{M}})$ of $\mathcal{M}$ are computed, the eigenpairs of $\mathcal{L}$ can be obtained by inverting the exponential transformation:

$$\begin{aligned}\lambda_{\mathcal{L}} &= \frac{\log|\lambda_{\mathcal{M}}| + i\arg(\lambda_{\mathcal{M}})}{\tau} \\ \boldsymbol{x}_{\mathcal{L}} &= \boldsymbol{x}_{\mathcal{M}}\end{aligned} \tag{12}$$

In this formulation, two specific numerical parameters have to be tuned, apart from those of the CFD solver: ϵ and τ. The finite difference parameter ϵ has to be large enough to avoid round-off errors, but not too large to prevent nonlinear effects. There is no general rule to set this parameter. For example, Bagheri et al. [30] recommend $\epsilon \in [0.01; 1]$, whereas Fosas de Pando et al. [31] use $\epsilon \in \{10^{-8}; 10^{-5}; 1\}$. Others like An et al. [32], instead, set ϵ as a function depending on both the base state and the perturbation. In our simulations, we have set $\epsilon \approx 10^{-6}$. Regarding the parameter τ, it must be smaller than half the oscillation period of the mode, in order to avoid aliasing effects and large enough to filter out numerical disturbances. The stability solver has been successfully validated against literature in the 2D cases of the lid-driven cavity (LDC) and the flow past a circular cylinder (see Appendix for details).

III. Stability of the NACA0012 Airfoil Wake

In this section, the 2D linear stability analysis on the NACA0012 airfoil is presented. The configuration of the current simulations is depicted in Fig. 1. The upstream velocity is imposed as $\boldsymbol{U} = U_\infty \cos \alpha \boldsymbol{e}_x + U_\infty \sin \alpha \boldsymbol{e}_y$, where α is the angle of attack. The airfoil closes at chord $C = 1$, with a sharp trailing edge, and the chord is taken as the characteristic length scale, i.e., $L = C$. Both the upper and lower edges of the domain are divergent to allow simulations at different angles of attack. To validate the present simulations, Table 1 summarizes the growth rate and mode frequency of the most unstable modes, obtained at different Reynolds numbers for the incompressible case at $\alpha = 16°$ and compared with the results of Zhang and Samtaney [33]. The authors have performed a biglobal stability analysis on the incompressible flow around a NACA0012 profile at $\alpha = 16°$, studying both the 2D and 3D cases by varying the transverse wavenumber value. They also conducted a 2D DNS tracking the early time evolution of the cross-stream velocity when the filtered base state is perturbed by a small-amplitude perturbation. The comparison shows a good agreement between present results and the reference. For the stability analysis the value of τ has been set to 0.1 characteristic time and a Krylov subspace of dimension $m = 300$ has been considered.

A. Incompressible Case

1. Influence of the Angle of Attack

The incompressible case has been simulated using a Mach number of 0.05. We first consider the unfiltered base flow whose mean aerodynamic coefficients C_D and C_L and corresponding Strouhal number St are reported in Fig. 2 for different angles of attack at $Re = 1000$. The results are in very good agreement with those of Kurtulus [34]. It can be observed from the St versus α plot that, at this Reynolds number, the onset of vortex shedding occurs at $\alpha = 8°$. The Strouhal number initially reaches values of the order of 0.9 before decreasing as α increases. This decrease shows that St scales with $C \times \sin \alpha$, which corresponds to the vertical distance between leading and trailing edge separated shear layers and hence represents a characteristic length scale for the interactions of shear layers across the wake. The onset of vortex shedding is found to be correlated with an increase in C_L, which reflects the separation and roll-up of the leading-edge shear layer and the influence of subsequent leading-edge vortex formation on the upper surface of the airfoil. Note that this trend in C_L versus α curve is different from that observed at higher Reynolds numbers, where leading-edge separation is generally associated with lift stall. Accordingly, because the leading-edge vortex generates a pressure force that acts normally to the surface, C_D is also found to increase more strongly for α values above 8°.

In Fig. 3a the growth rate versus frequency of the most unstable mode at different angles of attack is presented for $Re = 1000$. It shows a non-monotonic behavior of the growth rate ω_r with respect to α : a sharp increase as the angle of attack increases from 8 to 14°, where ω_r is maximal, followed by a decrease for $\alpha \geq 14°$. The frequency of the mode ω_i, instead, constantly decreases. Although this appears to correlate with the evolution of the natural frequency (see Fig. 2), we stress the fact that stability analysis is here performed on the filtered base flow and that, for such a base flow, the frequency of the most unstable mode does not accurately match the vortex shedding frequency away from the stability threshold.

Table 1 Growth rate and frequency ($\omega_r + \omega_i i$) with respect to Reynolds number at $\alpha = 16°$ compared with reference results

Re	Current work	2D DNS [33]	Biglobal analysis [33]
400	$0.2591 + 0.4555i$	$0.2754 + 0.4549i$	$0.2956 + 0.4285i$
600	$0.5164 + 0.4468i$	$0.5363 + 0.4459i$	$0.5126 + 0.4264i$
800	$0.6393 + 0.4261i$	$0.6625 + 0.4247i$	$0.6202 + 0.4085i$
1000	$0.6949 + 0.4012i$	$0.7160 + 0.3994i$	$0.6783 + 0.3860i$

The decrease in ω_i can be correlated with an increase in size of the recirculation region of the base flow, in both streamwise and transverse directions, hence an increase in the wake characteristic length scale, as depicted in Fig. 4. The length of the recirculation region is here identified using zero streamwise velocity isolines. Moreover, the streamwise wavelength of the most unstable mode increases with the thickening of the recirculation region associated with the increase of the angle of attack. The corresponding streamwise wavenumber is found to be proportional to the mode frequency, leading to a relatively constant phase velocity $v_\phi \approx 0.8$ with respect to α. This value scales with the base flow mean velocity measured in the wake well downstream of the recirculation bubble.

Figure 4 further shows that the spatial structure of the most unstable mode exhibits largest intensities in the wake downstream of the recirculation region for all angles of attack. The streamwise positions of maximal intensities of the mode are indicated by the red circles and are calculated considering the position of maximal amplitude of the envelope of the signal, i.e., the modulus of the complex signal. Yet, it is observed that the relative position between peak intensity and the recirculation region strongly varies with α. For $\alpha = 8°$, largest intensities are observed far downstream of the recirculation region, quite similarly to what can be observed behind bluff bodies at Reynolds numbers slightly above the stability threshold, i.e., critical Reynolds number corresponding to the first Hopf bifurcation [33,35]. The base flow in this region is nearly parallel, and the instability can be explained by deficits of streamwise velocity in the wake and the associated inflection points in their transverse distribution. The location of maximal intensity in the spatial structure of the most unstable mode and the tail end of the base flow recirculation region get closer as α increases.

This is further highlighted on Fig. 3b, which plots the streamwise position of the most downstream point of the recirculation region and that of peak intensity in the spatial structure of the most unstable mode. It is shown that the two regions first exhibit strong correlation at $\alpha \approx 12°–14°$, where the trend of the peak intensity position changes and starts increasing with respect to α, then both curves join at $\alpha = 18°$. The two regions seem uncorrelated below $\alpha = 14°$ and strongly correlated above. For $\alpha \geq 14°$, the most unstable mode is preferentially located in the nonparallel region of the base flow, and hence the mechanism driving the instability may differ from that at lower α. We note that $\alpha = 14°$ also corresponds to maximal growth rate of the unstable mode (see Fig. 3a), but it remains unclear at this

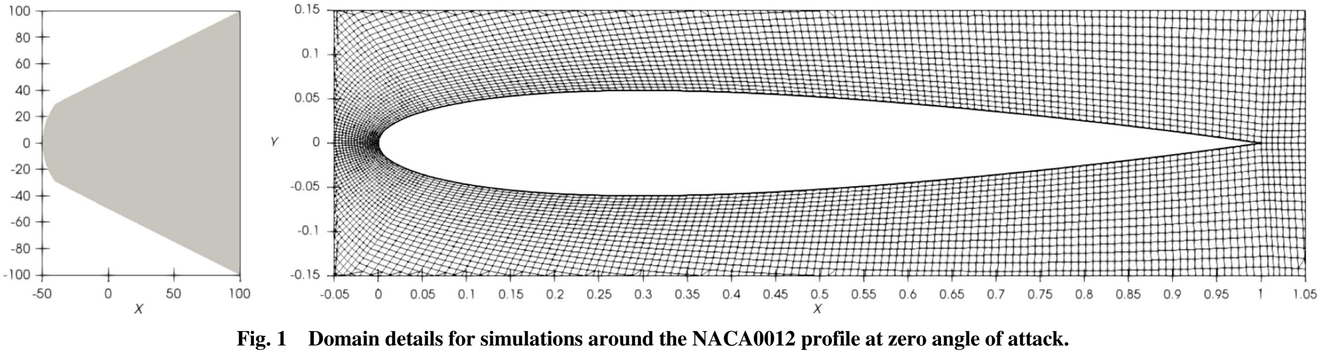

Fig. 1 Domain details for simulations around the NACA0012 profile at zero angle of attack.

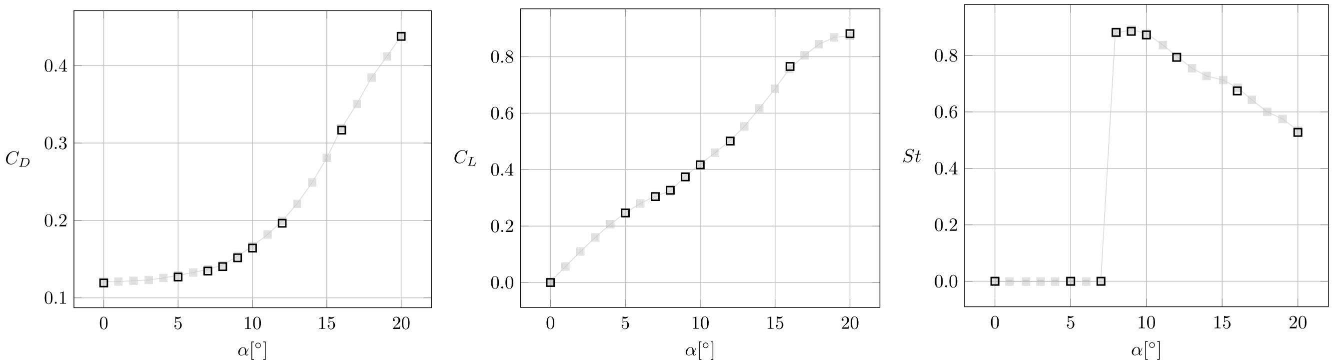

Fig. 2 Evolution of the mean values of C_D, C_L, and Strouhal number St with α at $Re = 1000$. Black marks show present results and light gray those of Kurtulus [34].

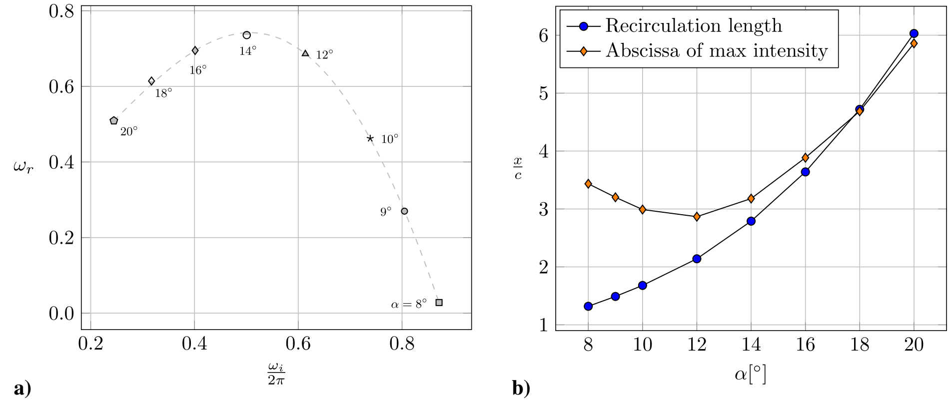

Fig. 3 Growth rate as a function of frequency of the most unstable mode (a) and length of the recirculation region and streamwise location of maximal intensity in the spatial structure of the most unstable mode (b), at $Re = 1000$ and varying α.

point whether or not the decrease of growth rate observed for $\alpha \geq 14°$ is due to the interaction between the recirculation region and the mode.

For the flow past square and circular cylinders, Mao and Blackburn [35] attributed the maximum growth rate to the base flow being most parallel at the end of the recirculation region. A measure of parallelism in this region was provided by the closing angle of the recirculation region, quantified by the ratio between the streamwise distance from the widest point to the end of the recirculation region (L) and its maximum width (H), as it is shown in Fig. 4. Although not shown here for the sake of conciseness, we also find that this ratio is maximal (i.e., the flow is most parallel at the end of the recirculation region) when the growth rate is maximal, which seems to corroborate previous observations of Mao and Blackburn. However, we will see in the next section that this hypothesis may not strictly hold for all cases.

2. *Influence of the Reynolds Number*

The evolution of ω_r as a function of ω_i for the most unstable mode at different Reynolds numbers and for $\alpha = 20°$ is displayed in Fig. 5a. The mode frequency slightly increases close to the stability threshold, i.e., from $Re = 200$ to $Re = 300$; this is probably due to the thinning of the shear layers, caused by the decrease of viscosity, which at those very low Reynolds numbers may impact the frequency more than the elongation of the recirculation region. Beyond $Re = 300$, instead, the mode frequency decreases, and the growth rate exhibits a nonmonotonic trend with a maximum observed around $Re = 800$.

It can be observed from Fig. 6 that the recirculation region extends further downstream with increasing Re, which is in line with previous observations on circular and square cylinders [35] and on the NACA0012 airfoil at $\alpha = 16°$ [33]. This supports the idea that the characteristic length scale of the recirculation region drives ω_i. The evolution of the streamwise wavenumber with respect to Re is also in line with the results of Mao and Blackburn [35] for the square cylinder: it slightly increases close to the stability threshold and drops as the Reynolds number is further increased. The wavenumber is proportional to the mode frequency, leading to a constant phase velocity $v_\phi \approx 0.8$, which is similar to what has been observed at constant $Re = 1000$ for the different angles of attack. Overall, Figs. 5b and 6 indicate that the evolution of the most unstable modes with Re is somewhat similar to that with α.

Figure 6 further shows that the end of the recirculation region and the streamwise abscissa of maximal intensity in the spatial structure of mode, indicated by the red circles, are clearly separated at $Re = 200$ and then get closer to one another as Re is increased. Figure 5b shows that the Reynolds number at which both locations first exhibit strong correlation is $Re \approx 400$–500, but the peak intensity joins the recirculation region at $Re = 800$, which corresponds to the maximum growth rate. This suggests that the interaction between the recirculation region and the far wake instability is a necessary condition, but not (solely) responsible for the change in the trend of ω_r as we move away from the stability threshold. On the other hand, we find again that the maximum growth rate is obtained when the base flow is most parallel at the end of the recirculation region, as measured by the closing angle defined previously.

Figure 7 summarizes these results in the form of contours of ω_r in the plane (α, Re). WI and RBI labels are added to denote regions of the parameter space where the dominant instability is located well downstream (wake instability) or at the end of the recirculation region (recirculation bubble instability) of the base flow. The thick red line delimits the two regions and is obtained by considering when the length of the recirculation region and the location of the mode peak intensity first exhibit strong correlation. The dashed black line marks the maximum growth rate obtained at each Re (as α is varied). For this range of Reynolds number and angles of attack, the maximum growth rate is always reached within the RBI region. The blue thick line

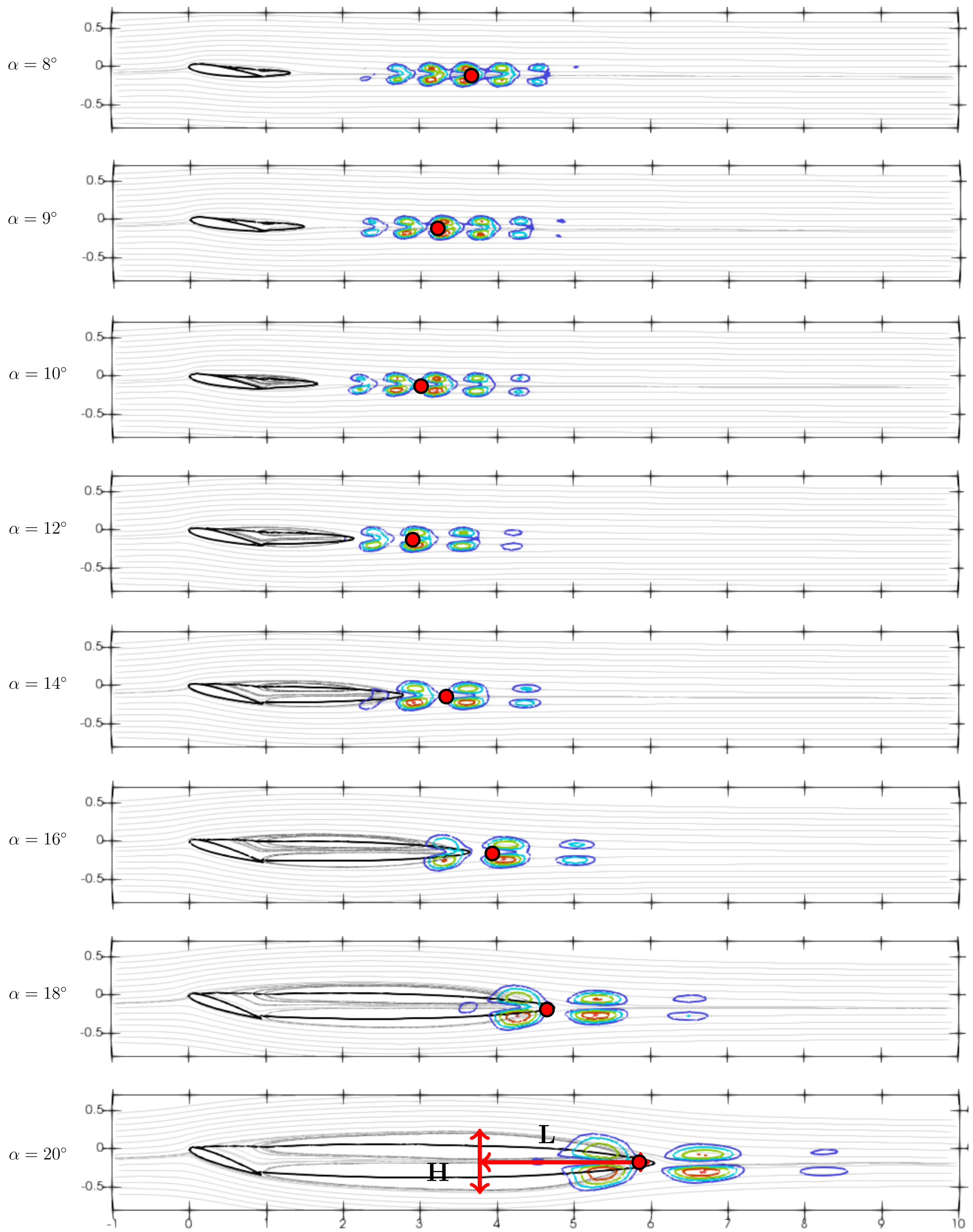

Fig. 4 $\|\widetilde{\rho u}\| / \max(\|\widetilde{\rho u}\|)$ isocontours at $Re = 1000$ and $M_\infty = 0.05$. Five levels of contours in the range $[0.5 - 1]$ are plotted. The base flow streamlines are in light gray and the solid black line corresponds to the isocontour $u_x = 0$. Red circles indicate the streamwise position of the peak intensity of the mode.

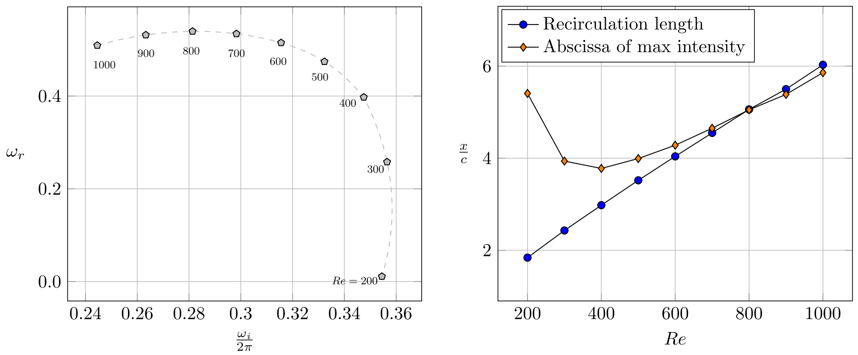

a) b)

Fig. 5 Growth rate as a function of frequency of the most unstable mode (a) and length of the recirculation region and streamwise location of maximal intensity in the spatial structure of the most unstable mode (b), for $\alpha = 20°$ and varying Re.

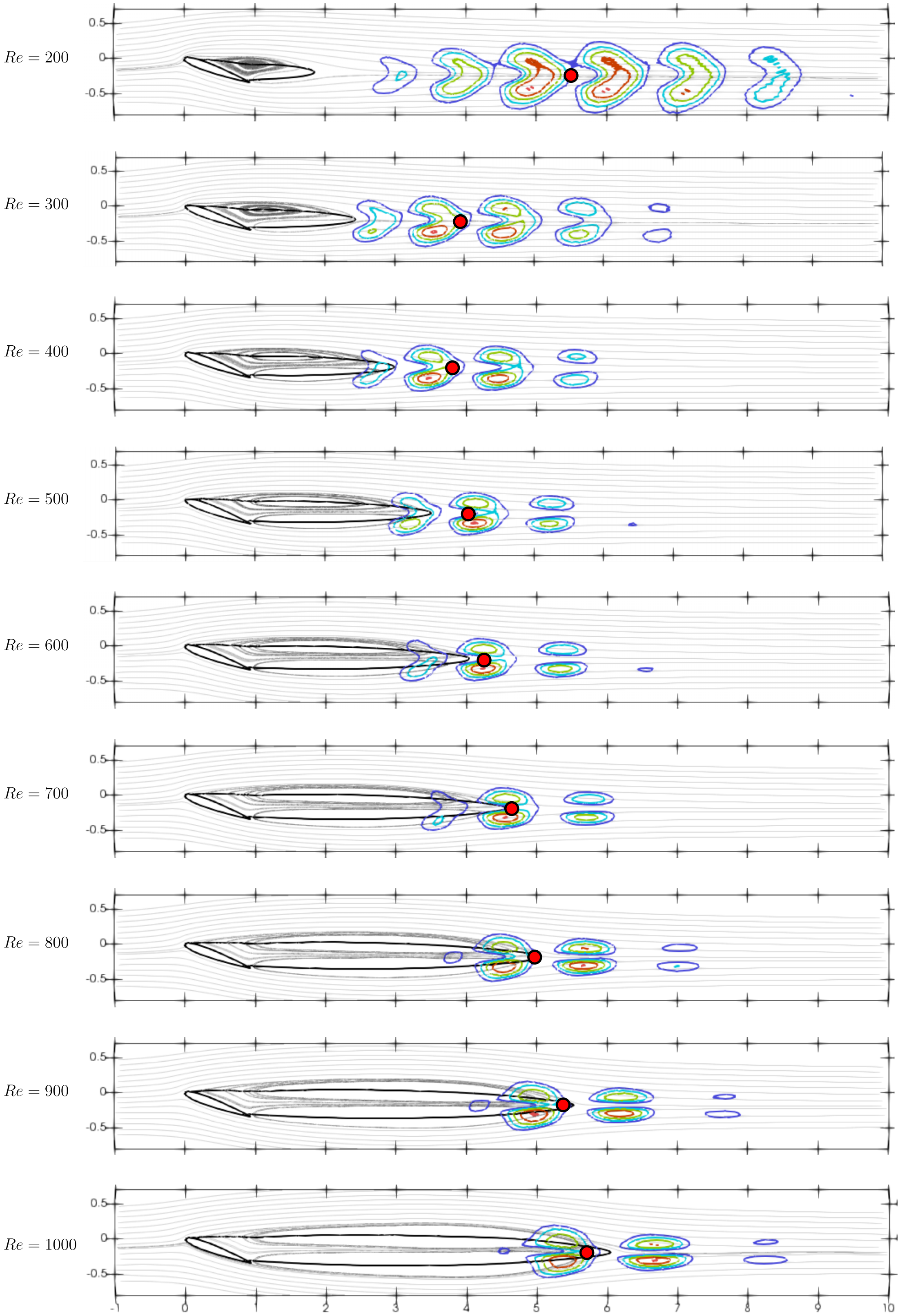

Fig. 6 $\|\tilde{\rho u}\| / \max(\|\tilde{\rho u}\|)$ isocontours at $\alpha = 20°$ and $M_\infty = 0.05$. Same conventions as in Fig. 4.

indicates when the base flow is most parallel at the end of the recirculation zone, measured by the maximum L/H ratio at each Re. This maximum is relatively close to that of the growth rate within the range of Re and α tested. Hence, Fig. 7 shows that ω_r reaches a maximum for all Re and that the angle of attack at which this value is obtained increases as Re decreases. Accordingly, the angle of attack at which the mode transitions from the WI to the RBI type increases as Re decreases. Moreover, it appears that within this range of Reynolds numbers, ω_r does not reach a maximum for all α and additional cases at higher Re should be computed to clarify whether ω_r continuously rises with Re or drops at some point. We note that the continuous increase in ω_r with Re is in line with previous results of

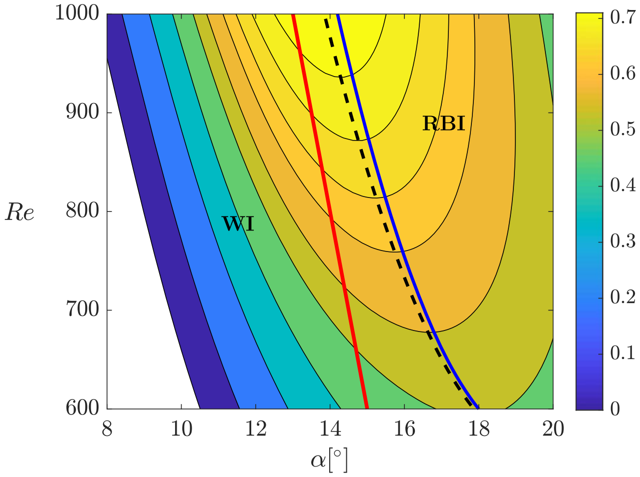

Fig. 7 Growth rate of the most unstable mode in the plane (α, Re). The dashed line corresponds to the maximum growth rate at each Re. The thick red line separates WI region from RCI region. The thick blue line corresponds to the maximum L/H ratio.

Zhang and Samtaney [33] obtained on the NACA0012 airfoil at $\alpha = 16°$ and $Re \in [400–1000]$. Finally, it can be observed that the variability of ω_r with α increases with the Reynolds number.

B. Compressibility Effects in the Subcritical Regime

The effect of compressibility on the aerodynamic coefficients is shown in Fig. 8 for a Reynolds number of $Re = 1000$ and various angles of attack. Both the drag and lift coefficients increase with the Mach number. This increase is more noticeable at high angles of attack and steepens with the Mach number, as expected. The Strouhal number, instead, decreases with the increase of M_∞ for all the tested angles of attack, except for $\alpha = 20°$, for which it increases with respect to the Mach number.

In Fig. 9a, the growth rate of the most amplified mode is shown as a function of its frequency at $Re = 1000$ for different angles of attack α and Mach number varying between 0.05 and 0.5. First, the frequency ω_i of this oscillatory mode decreases with α for all M_∞, which generalizes previous results on the incompressible case to the compressible one. In addition, ω_i decreases with M_∞ for all α. As discussed previously in the incompressible case, there is no strict correlation between the evolution of St and that of ω_i with respect to the Mach number, which can be attributed to our approach based on the filtered base state (rather than on the time-averaged base state). The decrease in ω_i with increasing M_∞ is consistent with previous works on bluff bodies [1,3,4,6,7] and can again be related to the elongation of the recirculation region. As illustrated in Fig. 10 for $\alpha = 16°$, the recirculation region of the base flow, depicted by the zero streamwise velocity contour in thick black line, elongates as the Mach number is increased.

On the other hand, the influence of compressibility on the growth rate of the most unstable mode depends on the angle of attack. For $\alpha = 8°$ and 9° the growth rate increases with the Mach number, indicating a destabilizing effect of compressibility that is clearly less pronounced for $\alpha = 9°$ than for $\alpha = 8°$. At $\alpha = 10°$, compressibility does not change the growth rate, whereas further increasing the angle of attack leads to a decrease of the growth rate with increasing Mach number, hence a stabilizing effect of compressibility. This figure further shows that the maximum growth rate (as α is varied) decreases with increasing M_∞ and it is achieved at slightly lower angles of attack compared with the incompressible case.

The transition between stabilizing and destabilizing effect of compressibility is also shown in Fig. 9b, where the characteristics of the leading mode are presented at $\alpha = 16°$ for different Reynolds numbers. Compressibility has a stabilizing effect at $Re = 1000$, 600, and 400, whereas it has a destabilizing effect at $Re = 300$, i.e., as one gets closer to the critical Reynolds number ($Re_c \approx 285$), leading to

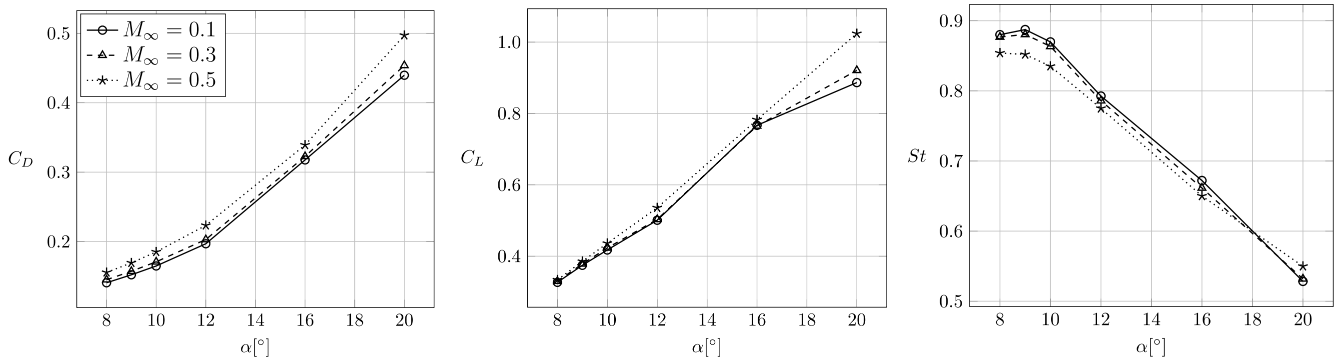

Fig. 8 Evolution of C_D, C_L, and Strouhal number St as a function of α at $Re = 1000$ and various M_∞.

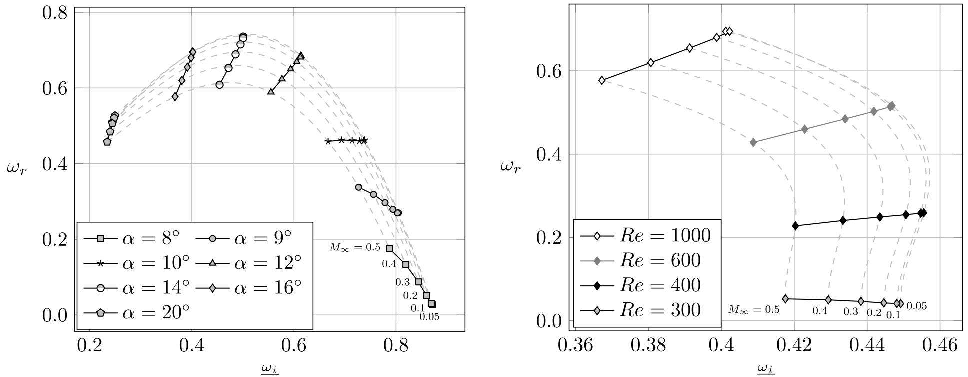

a) b)

Fig. 9 Most unstable mode evolution in the complex plane a) with respect to α and M_∞ at $Re = 1000$ and b) with respect to Re and M_∞ at $\alpha = 16°$. Dashed lines represent iso-Mach interpolation curves.

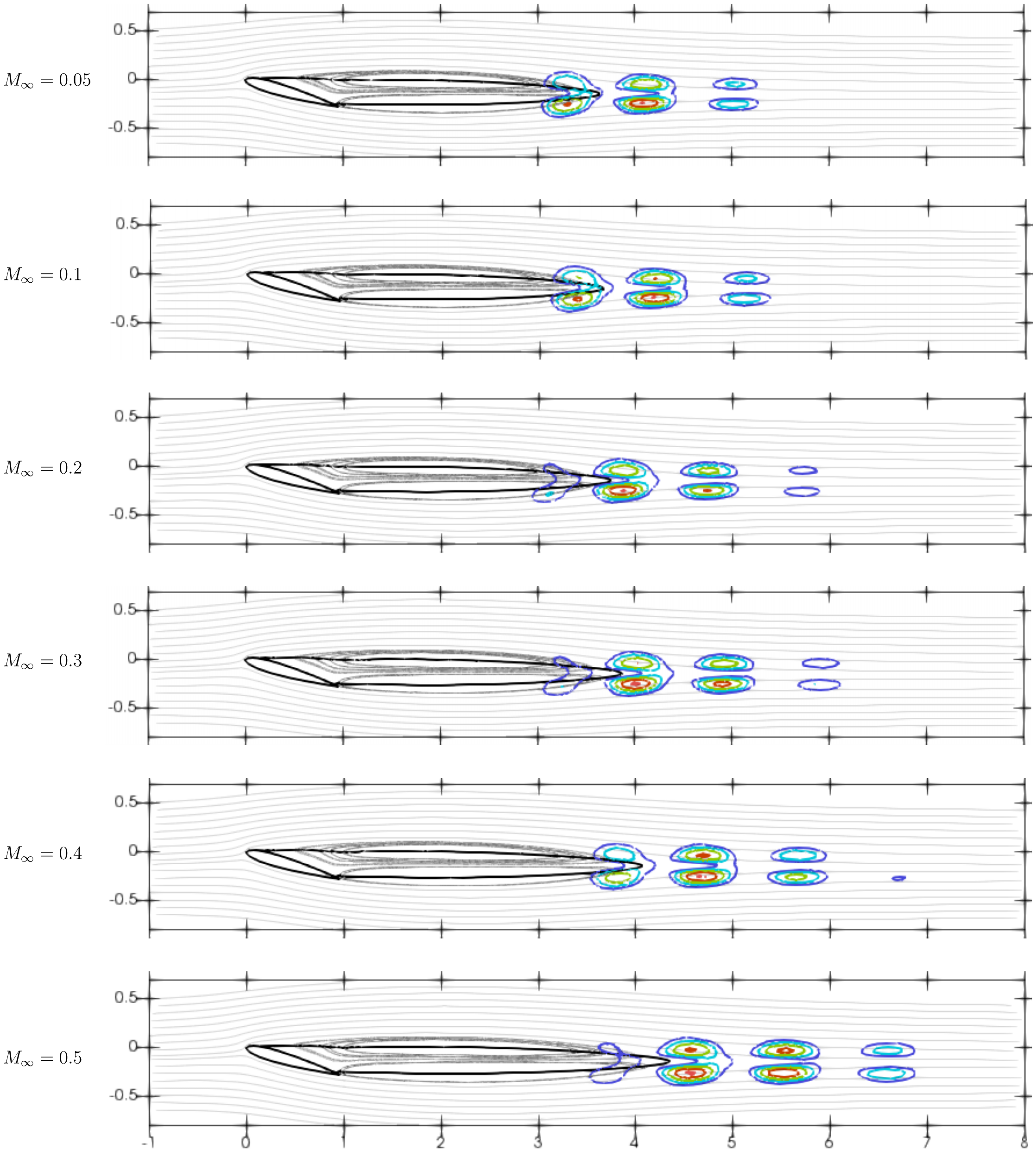

Fig. 10 $\|\rho\tilde{u}\| / \max(\|\rho\tilde{u}\|)$ isocontours at $\alpha = 16^\circ$ and $Re = 1000$. Same conventions as in Fig. 4.

the first Hopf bifurcation. Figure 11 summarizes the effect of compressibility on the most amplified mode in the plane (α, Re). The solid black line separates regions where compressibility has a stabilizing (S) effect from those where it has a destabilizing (D) effect. This limit goes from high to low Reynolds numbers as the angle of attack is increased, and it also shows that the destabilizing effect of the upstream Mach number is observed close to the critical threshold only.

In Fig. 12, the critical Reynolds number Re_c is presented as a function of the Mach number. Compressibility brings the first Hopf bifurcation forward for all the angles of attack considered here. Nevertheless, the intensity of the destabilization (the variation of ΔRe_c with M_∞) weakens as α increases: $\Delta Re_c = Re_c(M_\infty = 0.5) - Re_c(M_\infty = 0.05)$ represents 15%, 8% and 3% for $\alpha = 8^\circ$, 12°, and 16°, respectively, up to $\alpha = 20^\circ$, where compressibility does not influence the transition ($\Delta Re_c \approx 0$).

Through an adjoint-based sensitivity analysis, Meliga et al. [1] have analyzed the stabilizing/destabilizing effects of the Mach number on axisymmetric wake flows (sphere and afterbody) by

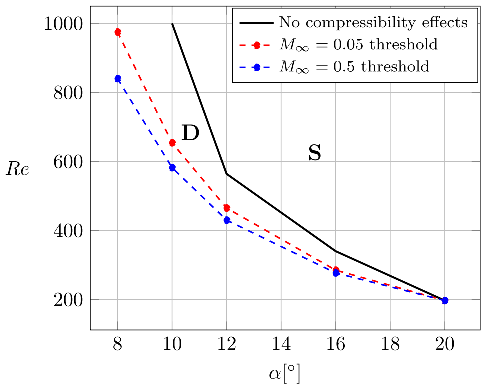

Fig. 11 Compressibility effects on the most amplified mode in the (α, Re) plane. The solid black line separates regions of stabilizing (S) and destabilizing (D) compressibility effect. The dashed lines correspond to the critical Re at $M_\infty = 0.05$ and $M_\infty = 0.5$.

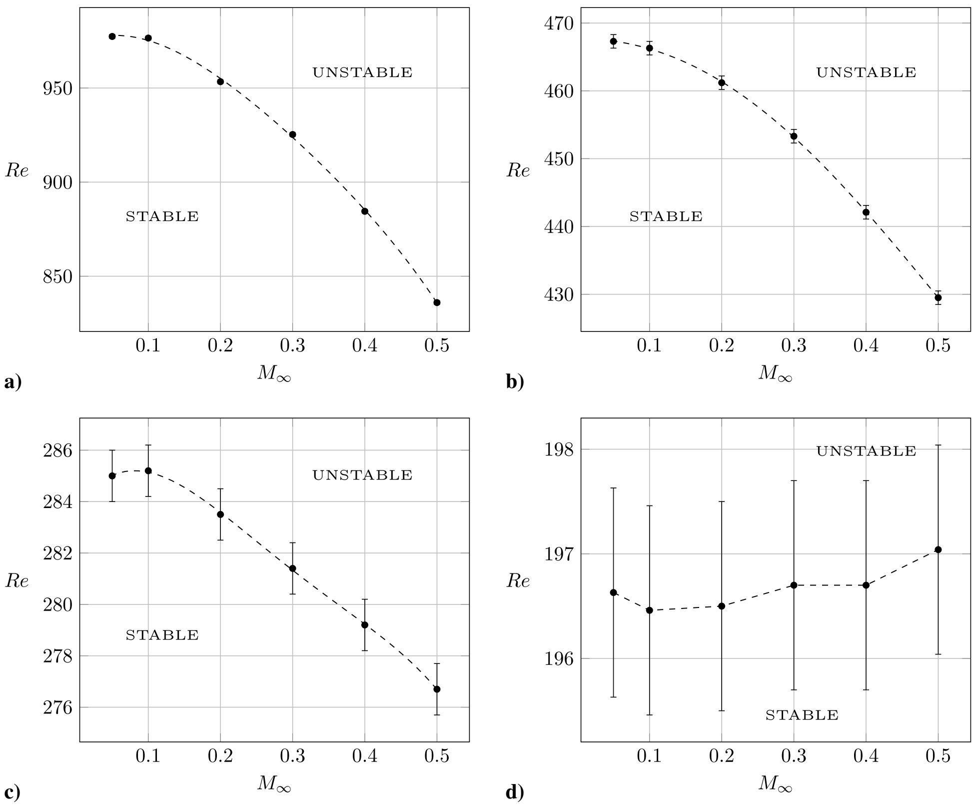

Fig. 12 **Neutral stability curves in the (M_∞, Re) plane for a) $\alpha = 8°$, b) $\alpha = 12°$, c) $\alpha = 16°$, and d) $\alpha = 20°$.**

considering the competition between the production, cross-stream, and streamwise advection of the disturbance by the base flow. In particular they have hypothesized that the destabilization is governed by the streamwise advection and is promoted when blockage effects are strong, i.e., when the width of the recirculation region is large compared with the characteristic length of the body. Yet, in our case, we find that blockage increases with α and that the intensity of destabilization (with increasing M_∞) decreases (see Fig. 12).

Nevertheless, the relation between blockage and the role of streamwise and crosswise advection may not be as straightforward. Figure 13 shows the spatial distribution of the base flow momentum variation with respect to the Mach number at $Re = 1000$. The streamwise momentum variation is negative downstream of the recirculation region, which promotes advection of the instability toward the recirculation bubble (destabilizing effect) for all the angles of attack. Its absolute value increases with α. The cross-stream momentum variation, instead, is significant only close to the recirculation bubble and tends to convect the instability away from the recirculation region (stabilizing effect). Looking at the location of the unstable mode relatively to the base flow recirculation region, the cross-stream momentum variation is likely to induce a stabilizing effect for $\alpha > 10°$ because the instability is close to the recirculation region; even if at $\alpha = 10°$, they do not present strong correlation yet. Conversely, for lower angles of attack, the instability is located far downstream of the recirculation region and is presumably not affected by such stabilizing effects. In a similar way, stabilizing

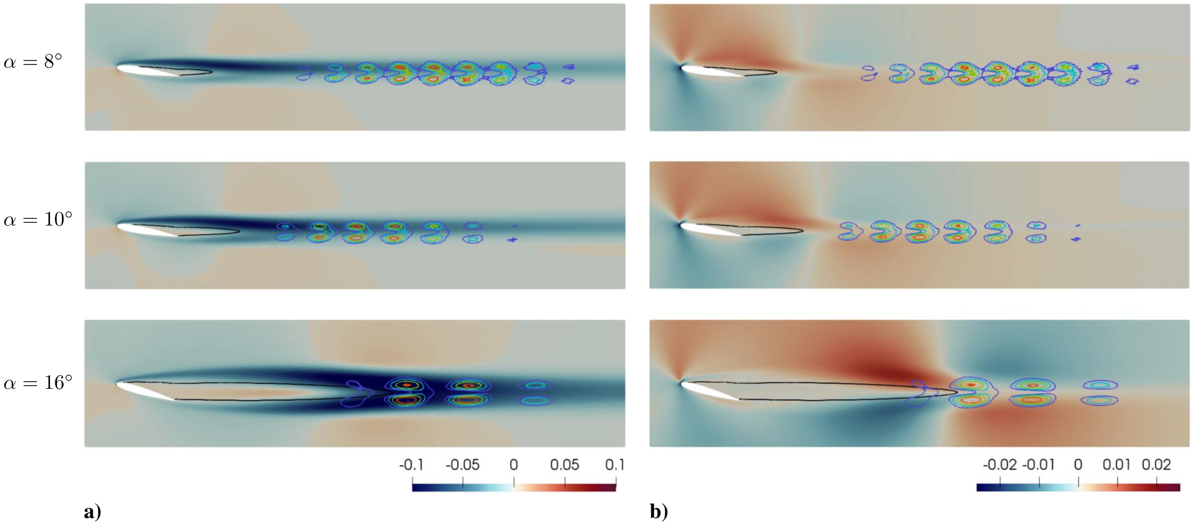

Fig. 13 **Momentum variation of the base state with respect to the M_∞ for different α at $M_\infty = 0.5$ and $Re = 1000$. Streamwise component $\partial \rho u_x / \partial M_\infty$ in column (a) and cross-stream component $\partial \rho u_y / \partial M_\infty$ in column (b). Same conventions as in Fig. 4.**

effects due to crosswise advection may not play a significant role at Reynolds numbers close to stability threshold, where the unstable mode is located far downstream of the recirculation region, at least for $\alpha < 20°$.

IV. Conclusions

Interest in low-Reynolds-number compressible flows has recently emerged together with prospective applications like stratospheric flight, Mars exploration, and vactrains. Up-to-date, very few studies have addressed this peculiar regime, and there is a lack of fundamental knowledge on the physics that drives compressible effects at low Reynolds numbers.

In this work, we have performed a global linear stability analysis, based on the finite volume spatial discretization of the compressible Navier–Stokes equations and Chiba's time-stepping approach, to gain insight into the mechanisms that govern wake instabilities behind a NACA0012 airfoil in the low-Reynolds-number compressible flow regime.

As a reference case, we first investigated the incompressible case ($M_\infty = 0.05$) at different angles of attack and Reynolds numbers. Our results indicate that the frequency of the most unstable mode decreases as α or Re increases, which is related to the elongation of the recirculation region of the (filtered) base flow, as previously observed on bluff bodies. Moreover, it has been observed that the growth rate of the most unstable mode first increases beyond the stability threshold with α or Re, before eventually decreasing. The instability first appears far downstream of the recirculation region, and the position of maximal intensity in the spatial structure of the mode gets closer to the airfoil, until the mode starts to interact with the recirculation region and then moves back downstream following the elongation of the recirculation zone; i.e., the mode transitions from a wake instability (WI) to a recirculation bubble instability (RBI). Nevertheless, the relative distance between the end of the recirculation region and the location of maximal intensity of the mode keeps decreasing. When Re is varied, the maximum growth rate is obtained when the peak intensity of the mode enters the recirculation zone. However, this is not as clear when α is varied, as the entry of the peak intensity into the recirculation zone is observed after the maximum value of growth rate has been reached. On the other hand, the maximum growth rate is observed when the base flow at the end of the recirculation region is most parallel and the instability is of RBI type, when both α and Re are varied. This somewhat generalizes results obtained on bluff bodies.

We then have investigated the effects of compressibility. Our results show that the general trends observed in the incompressible case hold for the subcritical regime. In particular, for all the Mach numbers investigated (i.e., up to 0.5), the frequency of the most unstable mode decreases with α and Re, which is again related to the elongation of the recirculation region of the base flow. Similar observations are made as M_∞ increases. Peak values in growth rate are found to occur when maximal intensities in the spatial structure of the most unstable mode are close to or on the recirculation region (RBI type). Moreover, it has been shown that the Mach number may have a stabilizing or destabilizing effect depending on α and Re. It was hypothesized that destabilizing effects of compressibility are due to an increase in negative streamwise advection (backward) of the disturbance by the base flow, on and downstream of the recirculation region, with increasing Mach number, whereas stabilizing effects result from an increase in crosswise advection on the recirculation region. Consequently, destabilizing effects are always nonnegligible, whereas stabilizing effects are significant in (or near) the RBI state, hence for Reynolds numbers and angles of attack far from critical values. This was further supported by Re versus M_∞ neutral stability curves obtained at different angles of attack.

As a future work, it would be interesting to explore further the influence of compressibility on the 3D instabilities developing on the 2D filtered base state, as done by Zhang and Samtaney [33] in the incompressible regime. The effect of an increasing Mach number on the development of 3D secondary instabilities that develop on the von Kármán vortex street could be also considered. This regime is still unexplored and may clarify on how compressibility changes the three-dimensionalization of the wake of the NACA0012 airfoil.

Appendix: Validation of the Stability Solver

A.1. Lid-Driven Cavity

The lid-driven cavity (LDC) consists of a square box of size L whose upper wall is a moving isothermal no-slip wall with constant tangential velocity U_∞ while the three other sides are fixed adiabatic no-slip walls.

All LDC simulations have been performed at $Re = 200$ and $M_\infty = 0.05$ in order to compare our results with those of Gómez et al. [36], who investigated the efficiency of the time-stepping approach on the incompressible LDC. To perform grid refinement analysis, three different meshes have been tested. The coarsest M1, medium M2, and finest M3 meshes have 48×48, 64×64, and 94×94 elements, respectively. In Fig. A1, the spectra obtained with mesh M2 and two different values of τ are presented. The cutoff frequency f_c given by

$$|f_c| = |\frac{\omega_{i_c}}{2\pi}| = \frac{1}{2\tau} \tag{A1}$$

for a given τ is clearly visible in the figure. Here, there are no mode with frequencies greater than $|f_c|$ ($|f_c| = 3.33$ for $\tau = 0.15$ and $|f_c| = 0.8$ for $\tau = 0.625$).

In Fig. A2a, the spectra obtained for different values of CFL number show that the time step does not influence the results, especially for the largest growth rates, as it can be seen in the close-up view of the spectrum displayed in Fig. A2b. The two stationary modes labeled Mode 6 and Mode 9 are those described in [36] and are used for validation. Their growth rates are reported in Table A1 for the different meshes and are in close agreement with those obtained by Gómez et al. [36].

Figure A3 presents the mesh convergence for the growth rate of these two modes together with the asymptotic value as given by the Richardson extrapolation. The values obtained with mesh M3 are correctly converged and the corresponding order of convergence is $p = 1.5$ and $p = 6.3$ for Mode 6 and Mode 9, respectively. Moreover, the values obtained with mesh M2 differ from the Richardson extrapolation by 1.2% for Mode 6 and by 0.1% for Mode 9. The structures of the modes are presented in Fig. A4 for mesh M2 and compared with those obtained by Gómez et al. [36]. The different isolines accurately match.

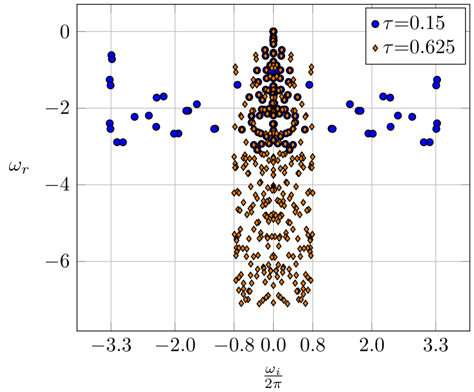

Fig. A1 Cutoff effect of τ on the spectrum of the LDC at $Re = 200$ and $M_\infty = 0.05$.

Table A1 Growth rate of Mode 6 and Mode 9 in comparison with the results of Gómez et al. [36]

Mode	M1	M2	M3	Gómez et al.
6	−0.3258	−0.3281	−0.3301	−0.3322
9	−0.5476	−0.5527	−0.5536	−0.5437

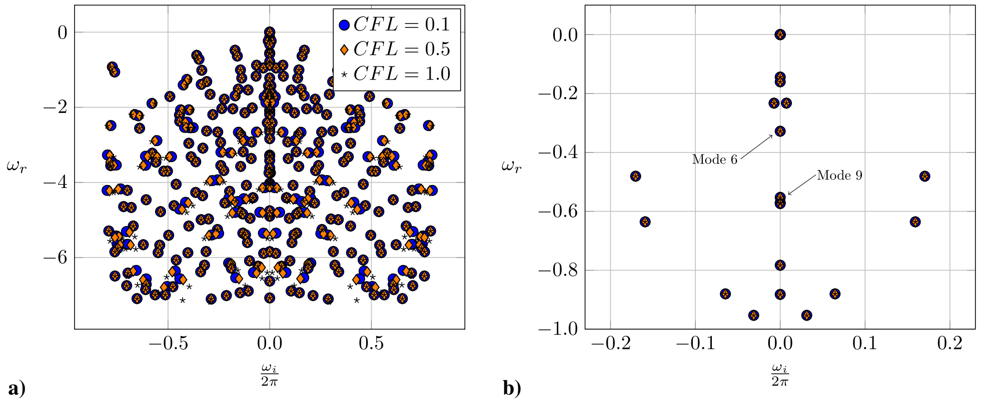

Fig. A2 a) Effect of CFL number on the spectrum of the LDC with $\tau = 0.625$ at $Re = 200$ and $M_\infty = 0.05$, and b) close-up view on the most relevant part of the spectrum.

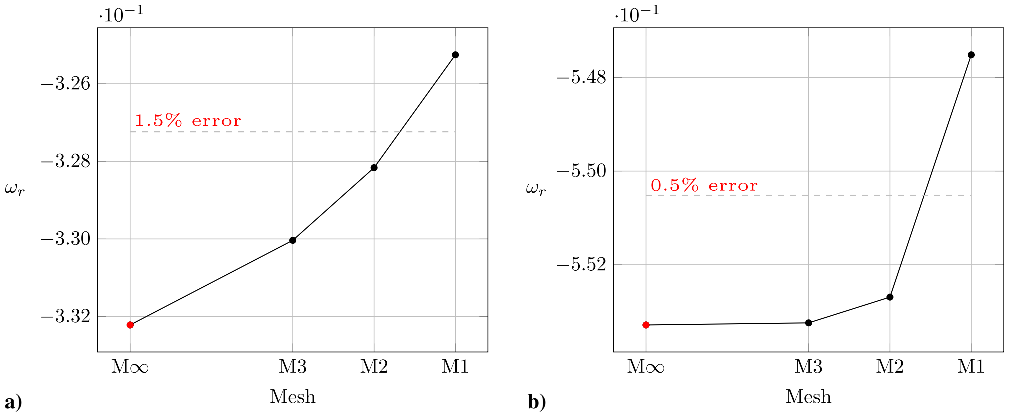

Fig. A3 Mesh convergence on the growth rate of a) Mode 6 and b) Mode 9. Red dots correspond to the Richardson extrapolation asymptotic values.

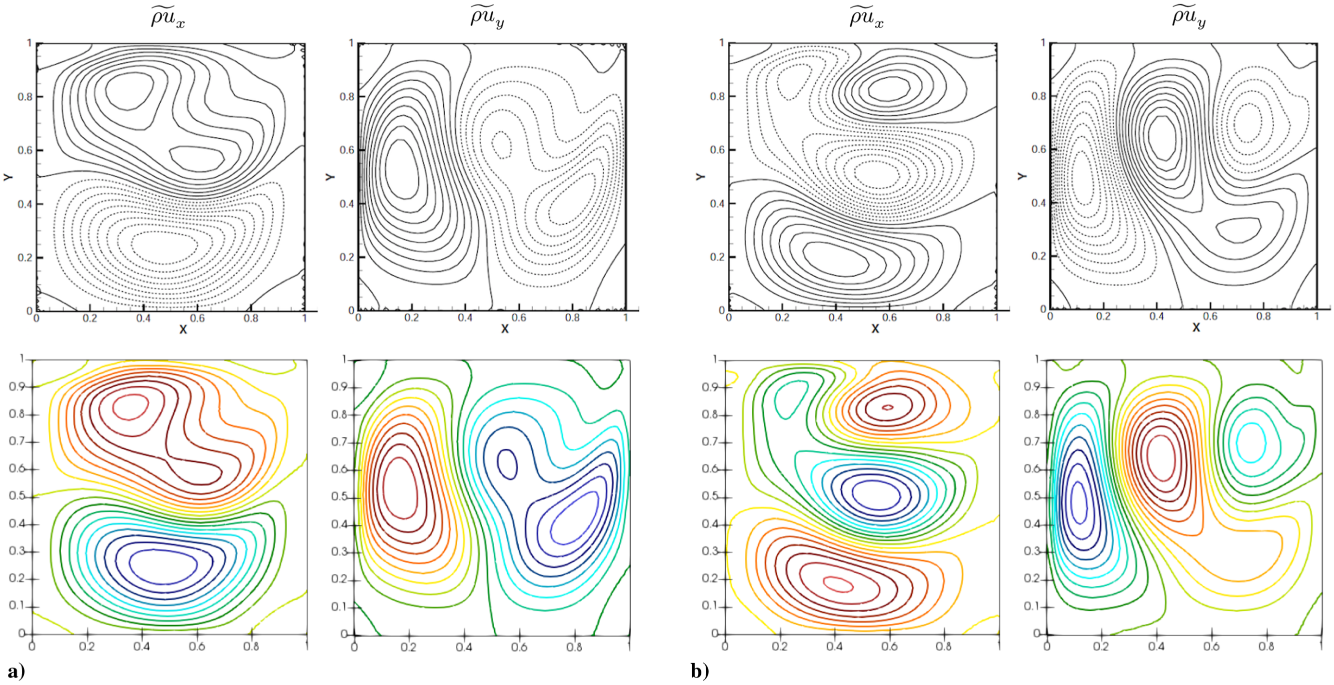

Fig. A4 Isocontours of a) Mode 6 and b) Mode 9. Upper and bottom lines correspond to results of [36] and present results, respectively.

In Fig. A5a, we consider the influence of both the integration time τ and the CFL number on the growth rate of Mode 6, for a Krylov subspace of dimension $m = 50$. We can see that, whatever the CFL, large values of τ are required to reach convergence, i.e., $\tau > 0.6$. In Fig. A5b, instead, the convergence of the growth rate of Mode 6 is presented for different values of the Krylov subspace dimension m at

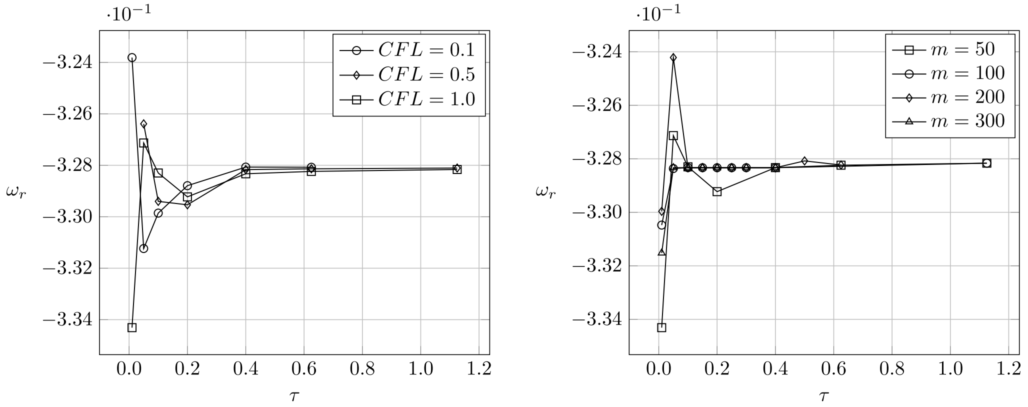

a) **b)**

Fig. A5 Convergence of the growth rate of Mode 6 with respect to τ for a) different CFL and $m = 50$ and b) for different m and CFL $= 1$.

CFL $= 1$. For low values of τ, the growth rate is very dependent on the Krylov subspace dimension, which is no longer true for higher values of τ.

A.2. Circular Cylinder

We now analyze the effect of compressibility on the stability of the 2D flow around a circular cylinder for different Reynolds numbers and compare our results with those of Canuto and Taira [3]. In their work, they obtained the complex frequency of the most unstable mode, by tracking the early time evolution of the lift coefficient of the unstable steady state computed with the SFD filtering technique and initially perturbed by a small numerical perturbation.

We firstly performed a domain sensitivity analysis. Two domains have been considered: a $40D \times 90D$ and a $40D \times 175D$ domain, where D is the diameter of the cylinder and is taken as the characteristic length scale, i.e., $L = D$. In Fig. A6a, the difference observed for the growth rates at $M_\infty = 0.2$ and $M_\infty = 0.3$ may be due to a lack of convergence for the results of Canuto and Taira as indicated by the non-monotonic behavior. Nevertheless, the characteristics of the most unstable mode obtained with both domains are in good agreement with the overall trend of the reference. For this reason, the simulations used to validate the compressibility effect have been performed on a $40D \times 90D$ domain. Moreover, the value of τ has been set to 0.5 characteristic time and the Krylov subspace dimension to $m = 300$.

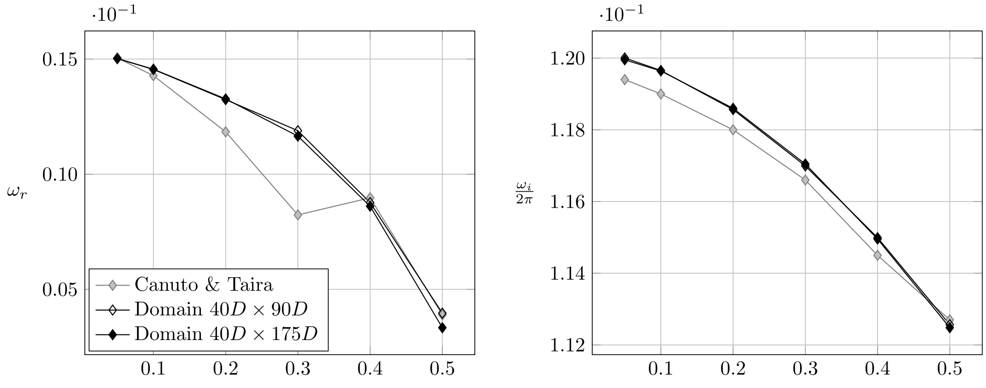

a) **b)**

Fig. A6 a) Growth rate and b) frequency of the most unstable eigenmode with respect to the M_∞ at $Re = 50$ for two domain sizes. Results of Canuto and Taira [3] are also reported.

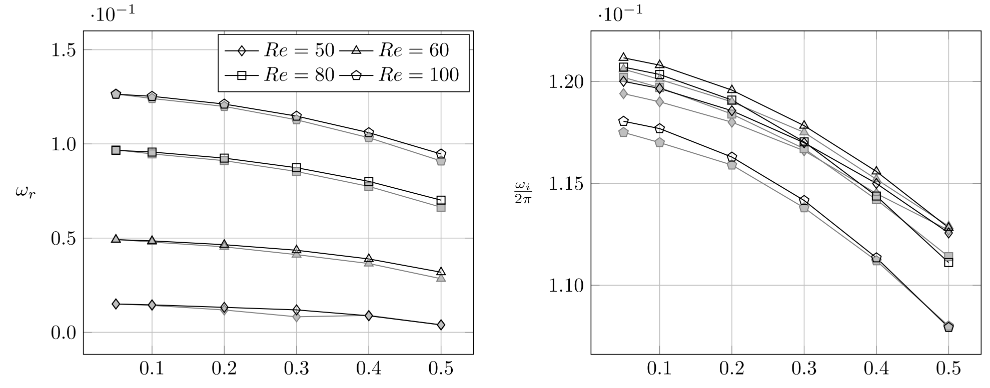

a) **b)**

Fig. A7 a) Growth rate and b) frequency of the most unstable eigenmode with respect to M_∞ for different Re. Gray lines correspond to results of Canuto and Taira [3].

In Fig. A7a, the growth rate and frequency of the most unstable eigenmode are reported with respect to Mach number for different Reynolds numbers together with the results of Canuto and Taira [3] in gray-colored lines. Overall, relatively good agreement is shown between both data sets. The stabilizing effect of the Mach number is clearly observed for all the Reynolds numbers considered, with growth rates decreasing as M_∞ increases. The mode frequency decreases as well with respect to the Mach number (see Fig. A7b), and this is found to be correlated with the elongation of the recirculation region that forms behind the cylinder, as observed in the base state, corroborating previous results by [3].

Acknowledgments

This work was performed using HPC resources from GENCI-IDRIS and GENCI-CINES on Jean Zay, Occigen (Grant A0082A07178), and CALMIP on Olympe (Grant 2020-p1425).

References

[1] Meliga, P., Sipp, D., and Chomaz, J.-M., "Effect of Compressibility on the Global Stability of Axisymmetric Wake Flows," *Journal of Fluid Mechanics*, Vol. 660, Oct. 2010, pp. 499–526. https://doi.org/10.1017/S002211201000279X

[2] Williamson, C. H. K., "Vortex Dynamics in the Cylinder Wake," *Annual Review of Fluid Mechanics*, Vol. 28, No. 1, 1996, pp. 477–539. https://doi.org/10.1146/annurev.fl.28.010196.002401

[3] Canuto, D., and Taira, K., "Two-Dimensional Compressible Viscous Flow Around a Circular Cylinder," *Journal of Fluid Mechanics*, Vol. 785, Dec. 2015, pp. 349–371. https://doi.org/10.1017/jfm.2015.635

[4] Sansica, A., Robinet, J.-C., Alizard, F., and Goncalves, E., "Three-Dimensional Instability of a Flow Past a Sphere: Mach Evolution of the Regular and Hopf Bifurcations," *Journal of Fluid Mechanics*, Vol. 855, Nov. 2018, pp. 1088–1115. https://doi.org/10.1017/jfm.2018.664

[5] Bouhadji, A., and Braza, M., "Organised Modes and Shock–Vortex Interaction in Unsteady Viscous Transonic Flows Around an Aerofoil Part I: Mach Number Effect," *Computers and Fluids*, Vol. 32, No. 9, 2003, pp. 1233–1260. https://doi.org/10.1016/S0045-7930(02)00100-7

[6] Nagata, T., Nonomura, T., Takahashi, S., Mizuno, Y., and Fukuda, K., "Investigation on Subsonic to Supersonic Flow Around a Sphere at Low Reynolds Number of Between 50 and 300 by Direct Numerical Simulation," *Physics of Fluids*, Vol. 28, No. 5, 2016, Paper 056101. https://doi.org/10.1063/1.4947244

[7] Nagata, T., Nonomura, T., Takahashi, S., Mizuno, Y., and Fukuda, K., "Direct Numerical Simulation of Flow Past a Sphere at a Reynolds Number Between 500 and 1000 in Compressible Flows," *2018 AIAA Aerospace Sciences Meeting*, AIAA Paper 2018-0381, 2018. https://doi.org/10.2514/6.2018-0381

[8] Gerrard, J., "The Mechanics of the Formation Region of Vortices Behind Bluff Bodies," *Journal of Fluid Mechanics*, Vol. 25, No. 2, 1966, pp. 401–413. https://doi.org/10.1017/S0022112066001721

[9] Liu, Z., and Kopp, G. A., "A Numerical Study of Geometric Effects on Vortex Shedding from Elongated Bluff Bodies," *Journal of Wind Engineering and Industrial Aerodynamics*, Vol. 101, Feb. 2012, pp. 1–11. https://doi.org/10.1016/j.jweia.2011.11.007

[10] Anyoji, M., Nose, K., Ida, S., Numata, D., Nagai, H., and Asai, K., "Low Reynolds Number Airfoil Testing in a Mars Wind Tunnel," *40th Fluid Dynamics Conference and Exhibit*, AIAA Paper 2010-4627, 2010. https://doi.org/10.2514/6.2010-4627

[11] Munday, P. M., Taira, K., Suwa, T., Numata, D., and Asai, K., "Nonlinear Lift on a Triangular Airfoil in Low-Reynolds-Number Compressible Flow," *Journal of Aircraft*, Vol. 52, No. 3, 2015, pp. 924–931. https://doi.org/10.2514/1.C032983

[12] Suwa, T., Nose, K., Numata, D., Nagai, H., and Asai, K., "Compressibility Effects on Airfoil Aerodynamics at Low Reynolds Number," *30th AIAA Applied Aerodynamics Conference*, AIAA Paper 2012-3029, 2012. https://doi.org/10.2514/6.2012-3029

[13] Désert, T., Jardin, T., Bézard, H., and Moschetta, J.-M., "Numerical Predictions of Low Reynolds Number Compressible Aerodynamics," *Aerospace Science and Technology*, Vol. 92, Sept. 2019, pp. 211–223. https://doi.org/10.1016/j.ast.2019.05.064

[14] Yang, H., and Agarwal, R. K., "CFD Simulations of a Triangular Airfoil for Martian Atmosphere in Low-Reynolds Number Compressible Flow," *AIAA Aviation 2019 Forum*, AIAA Paper 2019-2923, 2019. https://doi.org/10.2514/6.2019-2923

[15] Gómez, F., Clainche, S. L., Paredes, P., Hermanns, M., and Theofilis, V., "Four Decades of Studying Global Linear Instability: Progress and Challenges," *AIAA Journal*, Vol. 50, No. 12, 2012, pp. 2731–2743. https://doi.org/10.2514/1.J051527

[16] Theofilis, V., "Global Linear Instability," *Annual Review of Fluid Mechanics*, Vol. 43, No. 1, 2011, pp. 319–352. https://doi.org/10.1146/annurev-fluid-122109-160705

[17] Barkley, D., "Linear Analysis of the Cylinder Wake Mean Flow," *EPL (Europhysics Letters)*, Vol. 75, No. 5, 2006, p. 750. https://doi.org/10.1209/epl/i2006-10168-7

[18] Sipp, D., and Lebedev, A., "Global Stability of Base and Mean Flows: A General Approach and Its Applications to Cylinder and Open Cavity Flows," *Journal of Fluid Mechanics*, Vol. 593, Dec. 2007, pp. 333–358. https://doi.org/10.1017/S0022112007008907

[19] Turton, S. E., Tuckerman, L. S., and Barkley, D., "Prediction of Frequencies in Thermosolutal Convection from Mean Flows," *Physical Review E*, Vol. 91, No. 4, 2015, Paper 043009. https://doi.org/10.1103/PhysRevE.91.043009

[20] Bermejo-Moreno, I., Campo, L., Larsson, J., Bodart, J., Helmer, D., and Eaton, J., "Confinement Effects in Shock Wave/Turbulent Boundary Layer Interactions Through Wall-Modelled Large-Eddy Simulations," *Journal of Fluid Mechanics*, Vol. 758, Nov. 2014, pp. 5–62. https://doi.org/10.1017/jfm.2014.505

[21] Grébert, A., Bodart, J., Jamme, S., and Joly, L., "Simulations of Shock Wave/Turbulent Boundary Layer Interaction with Upstream Micro Vortex Generators," *International Journal of Heat and Fluid Flow*, Vol. 72, Aug. 2018, pp. 73–85. https://doi.org/10.1016/j.ijheatfluidflow.2018.05.001

[22] Åkervik, E., Brandt, L., Henningson, D. S., Hœpffner, J., Marxen, O., and Schlatter, P., "Steady Solutions of the Navier-Stokes Equations by Selective Frequency Damping," *Physics of Fluids*, Vol. 18, No. 6, 2006, Paper 068102. https://doi.org/10.1063/1.2211705

[23] Jordi, B. E., Cotter, C. J., and Sherwin, S. J., "An Adaptive Selective Frequency Damping Method," *Physics of Fluids*, Vol. 27, No. 9, 2015, Paper 094104. https://doi.org/10.1063/1.4932107

[24] Stewart, G. W., "A Krylov–Schur Algorithm for Large Eigenproblems," *SIAM Journal on Matrix Analysis and Applications*, Vol. 23, No. 3, 2002, pp. 601–614. https://doi.org/10.1137/S0895479800371529

[25] Arnoldi, W. E., "The Principle of Minimized Iterations in the Solution of the Matrix Eigenvalue Problem," *Quarterly of Applied Mathematics*, Vol. 9, No. 1, 1951, pp. 17–29. https://doi.org/10.1090/qam/42792

[26] Hernández, V., Román, J. E., Tomás, A., and Vidal, V., "Krylov-Schur Methods in SLEPc," Univ. Politecnica de Valencia TR STR-7, Valencia, Spain, 2007.

[27] Chiba, S., "Global Stability Analysis of Incompressible Viscous Flow," *Japan Society of Computational Fluid Dynamics*, Vol. 7, 1998, pp. 20–48.

[28] Tezuka, A., and Suzuki, K., "Three-Dimensional Global Linear Stability Analysis of Flow Around a Spheroid," *AIAA Journal*, Vol. 44, No. 8, 2006, pp. 1697–1708. https://doi.org/10.2514/1.16632

[29] Tezuka, A., "Global Stability Analysis of Attached or Separated Flows over a NACA0012 Airfoil," *44th AIAA Aerospace Sciences Meeting and Exhibit*, AIAA Paper 2006-1300, 2006. https://doi.org/10.2514/6.2006-1300

[30] Bagheri, S., Åkervik, E., Brandt, L., and Henningson, D. S., "Matrix-Free Methods for the Stability and Control of Boundary Layers," *AIAA Journal*, Vol. 47, No. 5, 2009, pp. 1057–1068. https://doi.org/10.2514/1.41365

[31] Fosas de Pando, M., Sipp, D., and Schmid, P. J., "Efficient Evaluation of the Direct and Adjoint Linearized Dynamics from Compressible Flow Solvers," *Journal of Computational Physics*, Vol. 231, No. 23, 2012, pp. 7739–7755. https://doi.org/10.1016/j.jcp.2012.06.038

[32] An, H.-B., Wen, J., and Feng, T., "On Finite Difference Approximation of a Matrix-Vector Product in the Jacobian-Free Newton–Krylov Method," *Journal of Computational and Applied Mathematics*, Vol. 236, No. 6, 2011, pp. 1399–1409. https://doi.org/10.1016/j.cam.2011.09.003

[33] Zhang, W., and Samtaney, R., "BiGlobal Linear Stability Analysis on Low-Re Flow Past an Airfoil at High Angle of Attack," *Physics of Fluids*, Vol. 28, No. 4, 2016, Paper 044105. https://doi.org/10.1063/1.4945005

[34] Kurtulus, D. F., "On the Unsteady Behavior of the Flow Around NACA 0012 Airfoil with Steady External Conditions at Re = 1000," *International Journal of Micro Air Vehicles*, Vol. 7, No. 3, 2015, pp. 301–326. https://doi.org/10.1260/1756-8293.7.3.301

[35] Mao, X., and Blackburn, H., "The Structure of Primary Instability Modes in the Steady Wake and Separation Bubble of a Square Cylinder," *Physics of Fluids*, Vol. 26, No. 7, 2014, Paper 074103. https://doi.org/10.1063/1.4887518

[36] Gómez, F., Gómez, R., and Theofilis, V., "Coupling Time-Stepping Numerical Methods and Standard Aerodynamics Codes for Instability Analysis of Flows in Complex Geometries," *6th Theoretical Fluid Mechanics Conference*, AIAA Paper 2011-3753, 2011. https://doi.org/10.2514/6.2011-3753

C. Lee
Associate Editor